Experimental and numerical investigation on integrated thermal management for lithium-ion battery pack with composite phase change materials

Yongqi Xie[a,*], Jincheng Tang[a], Shang Shi[b], Yuming Xing[a], Hongwei Wu[c,], Zhongliang Hu[d], Dongsheng Wen[a, d]**

[a]School of Aeronautic Science and Engineering, Beihang University, Beijing, 100191, China

[b]The 55th Research Institute, China Electronics Technology Group Corporation, Nanjing, 210016, China

[c]School of Engineering and Technology, University of Hertfordshire, Hatfield, AL10 9AB, United Kingdom

[d]School of Chemical and Engineering, University of Leeds, Leeds, LS1 9JT, United Kingdom

[*]Corresponding author. Email: xyq@buaa.edu.cn Tel. (86)10-82338081

[**]Corresponding author. Email: h.wu6@herts.ac.uk Tel. +44(0)1707284265

Abstract:

In this article, a novel composite phase change materials based thermal management system coupled with air cooling was proposed in order to sustain the temperature rise and distribution within desirable ranges of the lithium-ion battery utilized in a hybrid power train. A combined experimental and numerical study was conducted to investigate the effects of air flow rate and phase change material liquid fraction on the thermal behavior of the integrated thermal management system. Comparisons between the integrated system and an air cooling system were implemented under different air flow rates and ambient temperatures. Furthermore, thermal characteristics of both systems during charge-discharge cycles were numerically simulated. The results showed that the cooling effect of the integrated system was obviously better than that of the air cooling system. The variation of the air flow rate and ambient temperature had negligible impact on the heat dissipation of the phase change cooling. After the fully melt of phase change material, the battery temperature did not rise rapidly due to the auxiliary cooling of the cooling air. During 4C charge-discharge cycles, the temperature rise of the battery pack could be effectively restrained by the air cooling at a flow rate exceeding 300 m^3/h. While for the integrated system, good thermal management could be achieved with only 100 m^3/h of air flow rate. Especially for the operation mode, i.e., phase change material cooling during the discharge and coupled phase change material and air cooling during the charge, the integrated system could control the maximum temperature of the battery pack below 49.2 ^{o}C and reach up to six charge-discharge cycles under no additional battery power consumption.

Keywords: Lithium-ion power battery; integrated thermal management system; phase change material; air cooling; cycle characteristics.

Nomenclature

A	Heat exchange area, m^2
c	Specific heat, J/(kg·K)
h	Convective heat transfer coefficient, W/(m^2·K)
H	Enthalpy, J/kg
k	Thermal conductivity, W/(m·K)
L	Latent heat, J/(kg·K)
p	Static pressure, Pa
q	Heat generation rate of battery, W
Q	Volume flow rate, m^3/s
t	Time, s
T	Temperature, K
u	Velocity, m/s
V	Volume, m^3
ΔP	Pressure difference, Pa
ΔT	Temperature difference, K
β	Liquid fraction
ρ	Density, kg/m^3
μ	Dynamic viscosity, kg/(m·s)

Subscripts

amb	Ambient
b	Battery
dot	Per unit volume
f	Fluid
l	Liquid
max	Maximum
min	Minimum
p	Phase change material
ref	Reference
s	Solid

Acronyms

ACS	Air cooling system
CAD	Computer aided design
ITMS	Integrated thermal management system
PCM	Phase change material
PCSEU	Phase change storage energy unit
SOC	State of charge
TMS	Thermal management system

1. Introduction

In recent years, as the most suitable candidate for the hybrid electric vehicles and electric vehicles, the lithium-ion power batteries have attracted wide increased attentions due to their high specific energy density and long cycle life [1]. However, the performance of the lithium-ion batteries is significantly affected by the operating temperature. High operation temperature more than 55 ^{o}C can accelerate the battery ageing and shorten the lifespan [2]. It is recognized that the heat accumulation inside the battery will lead to a rapid temperature rise and even thermal runaway. The heat dissipation technology is limiting the commercial development of the large-scale battery pack [3]. It is therefore imperative to seek an effective thermal management system (TMS) in order to guarantee the battery can operate in the desired temperature range and keep as little temperature difference from cell to cell as possible [4].

Over the past two decades, many thermal management approaches have been studied, which mainly consist of air cooling system (ACS) [5], liquid cooling system [6], phase change material (PCM) cooling system [7] and heat pipe cooling system [8]. Due to the simple structure and low cost, ACS could be the earliest cooling technique that used for the battery thermal management. The experimental and numerical results investigated by Wu et al. [9] revealed that natural convection cooling could not effectively remove the heat from the battery pack whereas the forced convection cooling attained satisfactory the temperature rise of the battery. Park and Jung [10] numerically studied the effect of the battery cell arrangement on the thermal performance of the ACS and the parasitic power consumption. It was found that a wide battery module with a small cell to cell gap was desirable for the ACS. Under large heat load conditions, the consumed power of the ACS was much more than that of the liquid based TMS. Although a better cooling performance of the ACS could be achieved by means of the structure optimized design, the temperature difference in the battery pack was inevitable. Especially for large capacity and high discharge rate, the ACS could not effectively control the temperature rise and suppress the temperature difference of the battery [11].

It is well known that the liquid cooling can provide higher cooling efficiency and better thermal uniformity than the air cooling. The liquid cooling based TMS could maintain the battery temperature within a desirable range and the temperature difference from cell to cell is within 2 ^{o}C [12]. Transient thermal performance of a lithium-ion battery pack was analyzed by De Vita et al. [13] through comparing air cooling with liquid cooling strategy. By employing a liquid cooling based TMS on the basis of mini-channel cold plate, Rao et al. [14] numerically investigated the effect of various control factors, such as the number of channel, flow direction, coolant mass flow rate and ambient temperature on the temperature rise and distribution of the rectangular lithium-ion battery. For a cylindrical lithium-ion battery, they further studied the thermal performance of the mini-channel liquid cooling based TMS and found that the maximum temperature could be controlled under 40 ^{o}C as the number of mini-channel was no less than four and the inlet mass flow rate was 0.001 kg/s [15]. Afterwards, a series of research from the same research group revealed that the similar TMS with five mini-channels cold plate could achieve high cooling efficiency for the battery at 5C discharge [16]. Still liquid cooling based TMS has several disadvantages such as complex design, likelihood of leakage, high cost and difficult sustainment.

More recently, due to the extensive application in solar energy storage fields [17], the PCM based TMS that used to cool the battery are receiving increased attentions. It has simple structure, high latent capacity and no power consumption [18]. Al-Hallaj and Selman [19] took the lead in conducting the research on a battery module with a PCM based TMS. It was found that the temperature profile of the cells was substantially more uniform at different rates discharge than those without PCM. In the next study on a scaled-up battery pack, they [20] also presented that the PCM placed between the cells was able to be effectively used as a passive battery TMS without introducing moving components. However, the pure PCMs, such as paraffin, are not capable of meeting the demands of rapid heat storage owing to the low thermal conductivity.

Therefore, many studies have been carried out to enhance the thermal conductivity through adding metal foam, metal fins, or expanded graphite into paraffin [21]. The numerical investigations on the lithium-ion battery TMS made from pure octadecane, gallium and octadecane-Aluminum foam composite materials were carried out by Alipanah and Li [22]. It was stated that in comparison with the pure octadecane, adding Aluminum foam of 0.88 porosity to the octadecane led to 7.3 times longer discharge time and remarkably improved the uniformity of the battery surface temperature. Wilke et al. [23] conducted the nail penetration on a lithium-ion pack and studied the effectiveness of the TMS with and without phase change composite material. Their results showed that as a single cell entered thermal runaway, the TMS with PCM could prevent the propagation while the TMS without PCM could not. Compared to the TMS without a composite of PCMs and aluminum wire mesh plates, the thermal behavior of the LiFePO4 pack with the TMS was experimentally studied by Azizi and Sadrameli [24]. It was recognized that the maximum cell surface temperatures under ambient temperature condition were reduced by 19%, 21% and 26% at the rate of 1C, 2C and 3C, respectively.

With the increasing power and heat generation of the battery pack, single thermal management approach is not competent to meet the demand of the heat dissipation of the battery. As a consequence, the integrated thermal management system (ITMS) has become an important way to solve the problem of the battery thermal safety. So far, there are mainly several types of the ITMS, for instance, air cooling/PCM TMS, liquid cooling/heat pipe TMS and PCM/heat pipe TMS. Wu et al. [25] designed a heat pipe-assisted PCM based TMS and experimentally studied the thermal performance. Experimental results showed that the highest temperature of the battery could be kept below 50 ^{o}C even at 5C discharge and a more stable and lower temperature fluctuation was achieved at different cycling conditions. For a tube-shell lithium-ion battery pack with expanded graphite/paraffin composite, the thermal characteristics of the TMS coupled with forced air cooling were investigated experimentally and numerically by Jiang et al. [26]. It was found that the ITMS obviously reduced the cell temperature rise and kept the maximum temperature difference within a low value of 1~2 ^{o}C. Zou et al. [27] proposed an ITMS with heat pipe and studied its thermal performance under different working conditions. It was indicated that the system could meet the basic cooling demand. Lazrak et al. [28] conducted a combined experimental and numerical study to investigate the thermal performance of the ITMS based on PCMs and found that the ITMS could reduce temperature rise more than 5 °C and improve its distribution around the cell. Rao et al. [29] numerically investigated the thermal behavior of the PCM/mini-channel coupled TMS by analyzing the effect of the mass flow rate of water, phase change temperature, and thermal conductivity of PCM. The maximum temperature for the ITMS was 14.8 ^{o}C, which is smaller than that for PCM-based TMS.

To the best knowledge of the authors, there is still much room to study on extension for the TMS coupled with multi cooling approaches. In the current study, for a lithium-ion power battery pack used in the hybrid power train, an ITMS with PCMs and air conditioning exhaust was proposed. The thermal behaviors of the ITMS were investigated experimentally at different air flow rates, PCM melted rates and ambient temperatures. Comparisons between the ITMS and the pure ACS were also analyzed. Moreover, the thermal characteristics of both thermal management methods during charge-discharge cycle process were numerically simulated.

2. Experimental system and test section

An experimental test apparatus was built at Reliability and Environmental Engineering Laboratory at Beihang University, China. The experimental investigations on the thermal management performance of the lithium-ion battery pack with the ITMS were carried out.

2.1. Experimental system

Fig. 1 presents the diagrammatic sketch of the experimental system, which is mainly composed of the charge-discharge system, data acquisition system, thermal performance test system and the test section. The charge-discharge system was used to simulate the operation state of the battery under different charge and discharge rates conditions. It mainly included several programmable DC power supplies, programmable DC electric loads and relevant test and control software. During the charge period, the battery pack discharged to 18 V with constant currents of 2C/20A, 3C/30A and 4C/40A. During the discharge process, it firstly charged to the termination voltage of 33.6 V with constant currents of 2C, 3C and 4C and then charged at 33.6 V until the termination current of 0.05 A. In the experiments, the coulomb counting method [30] was selected to estimate state of charge (SOC) and the initial battery capacity during charge was assumed to be 0 Ah. During the middle stage of the charge and discharge, the linear relationship between the SOC and the charge-discharge time was supposed. In addition, the effect of the battery aging and the charge-discharge cycle was ignored.

The thermal performance test system provided the required cooling air velocity and ambient temperature, which mainly consisted of a variable frequency centrifugal fan (DF-4), electric heater, DC power supply (HSPY-600), air flowmeter (NRHLF0175), thermostat chamber and pipe. The centrifugal fan and electric heater were used to regulate the air flow and temperature, respectively. The air flow rate from 0.5 N m^3/h to 50 N m^3/h was measured by the air flowmeter with the accuracy of 50±0.25 N m^3/h. In order to reduce the heat leakage to the surroundings, the pipe was wrapped by the thermal insulation materials (Rubber Foam Thermal Insulation Sheet, 0.034 W/m·K) with the thickness of 10 mm. The test section, namely, the battery pack, was installed inside the thermostat chamber. In the current study, three different temperatures (28 ^oC, 35 ^oC and 42 ^oC) were selected to simulate the exhaust air of the air conditioner in the hybrid power train, the mixed air of exhaust air and outside fresh air, as well as the outside fresh air in summer.

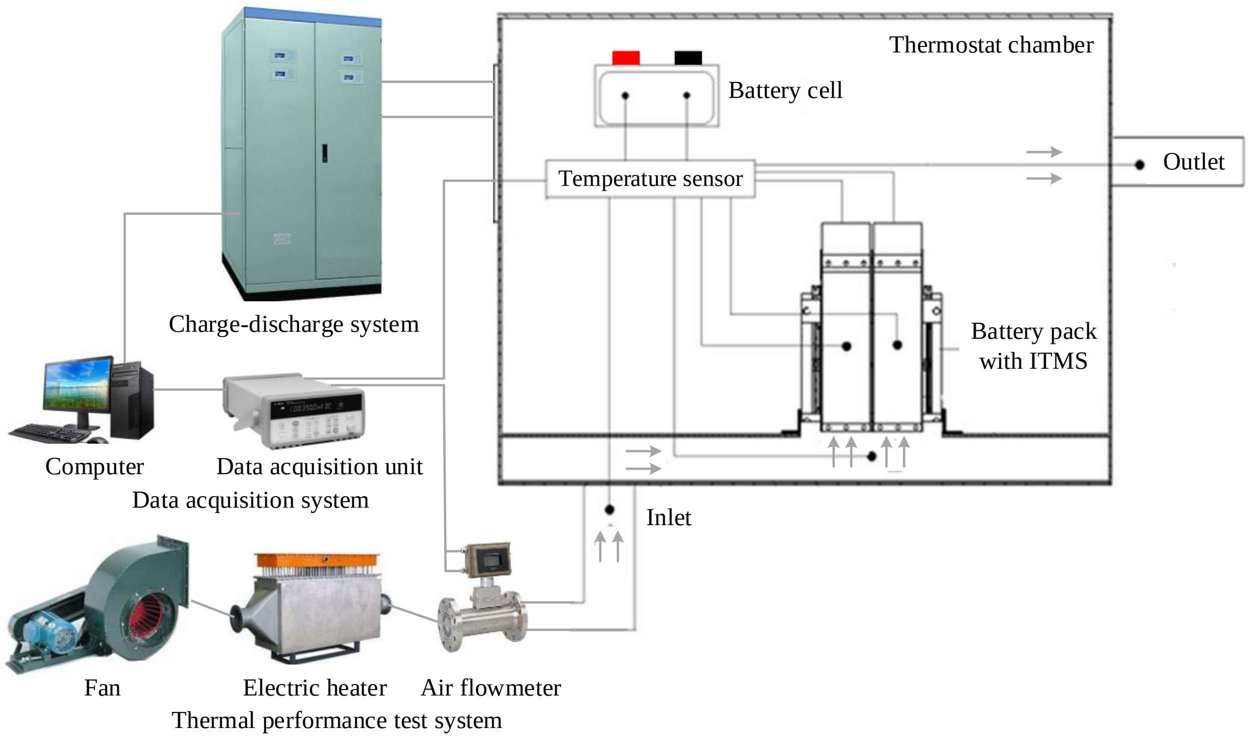

Fig. 1. The diagrammatic sketch of the experimental system.

The main components of the data acquisition system included six platinum temperature sensors (PT100, ±0.06 ^oC at 0 ^oC), a data acquisition unit (Agilent 34970A) and a computer. These temperature sensors were evenly arranged on the surface of the battery cell at three different positions inside the battery pack. There were two PT100s on the surface of each battery cell. The temperatures at different locations, air flow rate, charge-discharge current and voltage were recorded every second by using Agilent 34970A and saved in the computer.

2.2. Test section

Fig. 2 shows the schematic diagram and photo of the battery pack with the ITMS. The battery pack consisted of twelve pouch cells covered with an aluminum sheet of 0.35 mm thickness and thirteen porous structures (engineering plastic-ABS), which was 1/49 of the real battery pack in the hybrid power train. The cell was embedded in the porous structure which allowed the cooling air flow through. The specifications for the commercial lithium-ion battery cell provided by the manufacturer (Microvast Power Systems Co., Ltd.) are illustrated in Table 1.

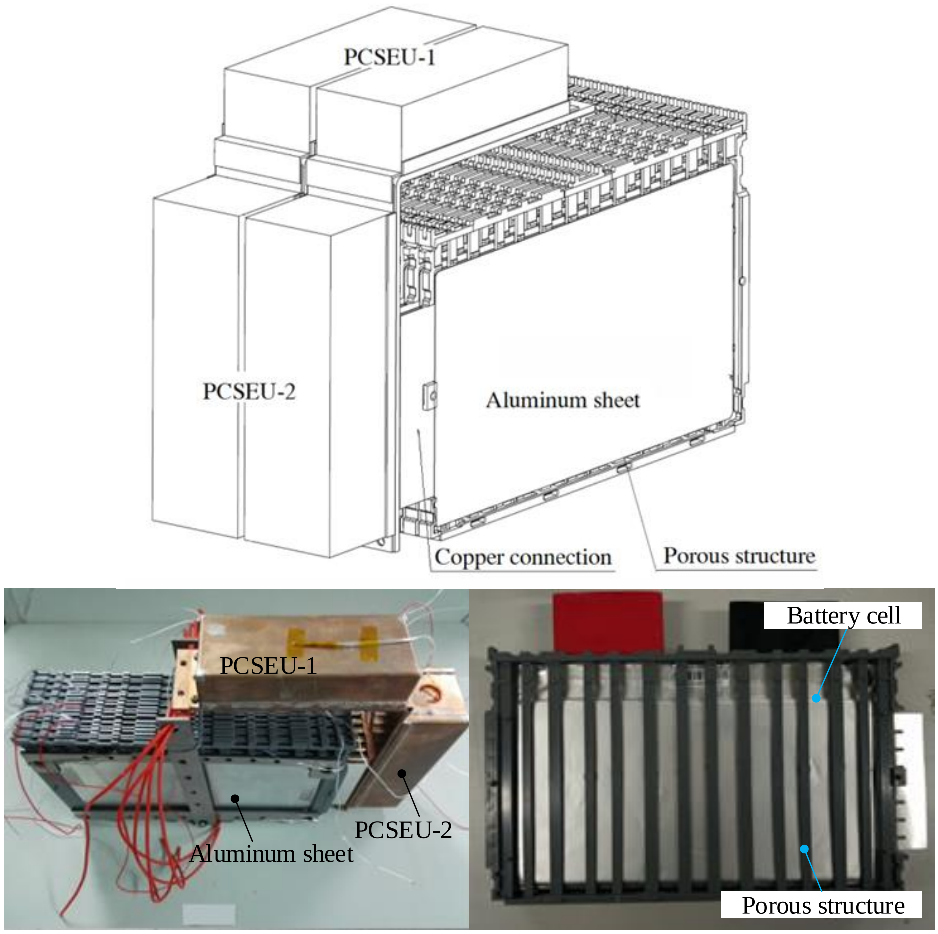

Fig. 2. Schematic diagram and photo of the battery pack with the ITMS.

Basically the ITMS includes four phase change storage energy units (PCSEUs), two L-shape copper collector plates, and twelve copper connecting fins. The outline dimensions of PCSEU-1 and PCSEU-2 were 120 mm × 45 mm × 30 mm and 145 mm × 45 mm × 45 mm, respectively. Both PCSEUs assembled on the collector plate with dimension of 160 mm × 45 mm × 2 mm were arranged on the side and top of the battery pack. The connecting fin with 1.5 mm thickness and 15 mm height was utilized to link the collector plate with aluminum sheet. The PCSEUs absorbed the heat generated by the battery through heat conduction. It is worth noting that the PCSEUs configuration had little impact on the cooling air flowing through the porous structure to cool the cells.

Table 1 Specifications for commercial lithium-ion battery cell.

Specifications	Value (unit)
Type	Lithium titanate battery
Dimensions	6.1 mm×203 mm×127 mm
Nominal voltage	2.3 V
Nominal capacity	10 Ah
Recommended temperature	-10 ~ +45 ºC (charge)
	-25 ~ +55 ºC (discharge)
Thermal conductivity of battery	5.22 W/(m·K)

On the basis of the application demands, the n-eicosane paraffin with purity of 99% was employed as the organic PCM. Its phase change temperature was from 36 ^{o}C to 38 ^{o}C and the latent heat was 241 kJ/kg. In order to enhance the thermal conductivity of the PCM, the copper foam with porosity of 95% was added to form the composite PCM with paraffin. The paraffin was heated to liquid and then was poured into the copper foam core. The thermal conductivity of composite PCM was 5.27 W/m·K, which was measured by Hot Disk Analyzer (TPS 1500) based on transient plane source method [31]. The composite PCM was encapsulated by welding with six copper plates with 1.0 mm thickness to form the PCSEU. In the current study, the PCSEUs were wrapped by the thermal insulation material (Rubber Foam Thermal Insulation Sheet, 0.034 W/m·K) in order to reduce the effect of the external air convection.

3. Mathematical model and model validation

This section primarily focuses on the development of the mathematical model of the entire battery pack, followed by governing equations and model validation.

3.1. Numerical description

In the hybrid power train, there were total 12 battery modules, which were evenly arranged in upper and lower layers in a cube box, as shown in Fig. 3. Some basic dimensions of the battery pack were also presented in Fig. 3. Each module consisted of 49 pouch cells and the total number of the cell was 588. Parallel ventilation was designed and the cells were cooled by the air flowing through the porous structure from the pack at the bottom.

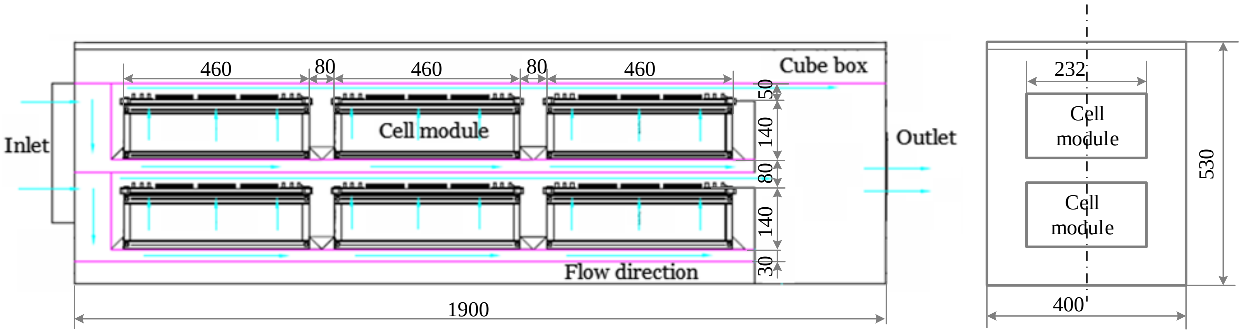

Fig. 3. Schematic of the entire battery pack (cube box).

The simplified physical model of the entire battery pack was created by the CAD software SolidWorks 2010. The interfacial thermal contact resistance between the collector plate and PCSEUs was considered as a thermal layer with 0.1 mm in thickness and 4.8 W/m·K in thermal conductivity. For other contact interfaces, perfect contacts were assumed. The computational domain of the entire battery pack and the local solid domain for cells and PCSEUs were presented in Fig. 4. In order to simplify the calculation, assuming that the cooling air was incompressible, the air flow field inside the battery pack was firstly resolved without considering the energy equation. Thus the velocity and pressure distributions around each cell were obtained. Afterwards, the energy equation was solved using the known velocity distribution as boundary conditions. Therefore, the temperature fields of all the battery cells could be achieved.

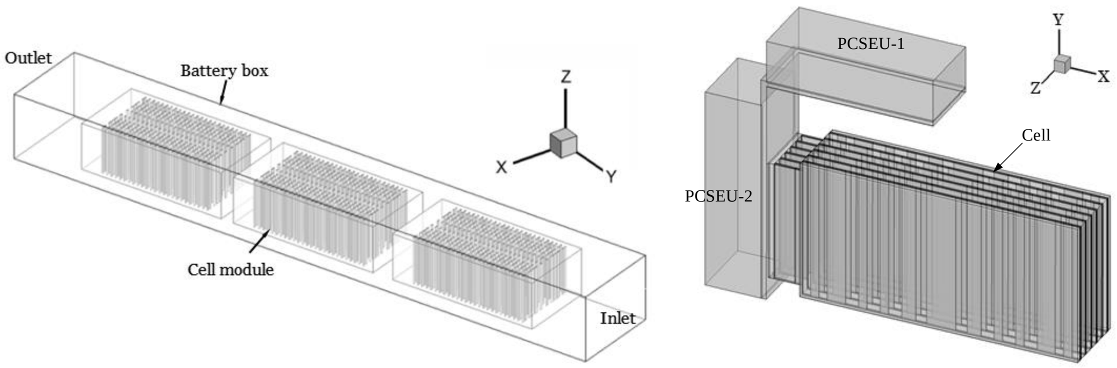

(a) The entire battery pack (b) Local domain for cells and PCSEUs

Fig. 4. The computational domain of the entire battery pack. (a) The entire battery pack. (b) Local domain for cells and PCSEUs.

The hexahedral meshes were created to discrete the computational domain using the software ICEM CFD 14.0. Local five boundary layers were generated at the cells and wall surfaces. Grid independent analyses were conducted to ensure the calculation results being independent of the grid size. The total grid number for the entire fluid domain and local solid domain, as shown in Fig. 4, was 4,201,988 and 954,463, respectively. Additionally, the model of the whole battery pack without the ITMS was also created for simulating the thermal behavior of the ACS.

In the current simulations, the radiation heat transfer was not taken into account [32]. The heat transfer between the battery box casing and surroundings was also negligible. For the composite PCM with copper foam and paraffin, the properties were assumed to be constant and identical for both liquid and solid phase [29, 32]. The motion of solid paraffin, the volume variation and the convective heat transfer between paraffin and copper foam were all neglected during the period of phase change [33]. Consequently, the melting of the composite PCM could be considered as pure thermal conductivity process. Focused on the thermal characteristics of the battery pack under harsh conditions, a high charge and discharge rate of 4C was used to for the simulation. Both charge and discharge times were approximate 900 s. In order to get the real results, the actual heat generation rate of the battery under 4C charge-discharge rate conditions was utilized, which was assessed to be uniform in each cell. Velocity inlet, pressure outlet and no-slip wall were set as the boundary conditions. The gauge pressure at the outlet was considered as zero gauge pressure. The air temperature at the inlet was set to 35 ^{o}C and 42 ^{o}C, respectively. The ambient conditions at 1 atmospheric pressure were used to initialize the computational domain. The initial temperatures of the cells and the PCSEUs were set to the ambient temperature. The time step was set as 1 s and the iteration number per time step was 60 so as to decrease the calculation time. The convergence criteria were set to 1×10^{-4} of the residuals for the continuity, momentum and energy equations. The walls on the top, side and bottom of the battery box casing were specified as adiabatic wall boundary conditions.

3.2. Governing equations

The heat generated by the battery originates from the combined effects of the internal electrochemical reactions and the electrical-heat transformation. During the charge and discharge process, the heat generation rate mainly includes irreversible Joule heat, reversible heat from the electrochemical reactions, heat from side reactions and heat of mixing [34]. According to the analysis of the heat transfer mode of the battery [35], the heat generation rate (q) can be calculated as follows.

$$q = hA\left(\frac{T - T_0}{1 - \exp\left(-\frac{hA}{\rho_b c_b V_b} t\right)} + T_0 - T_{amb}\right) \tag{1}$$

where h is the convective heat transfer coefficient, A is the heat exchange area, t is the time, T and T_0 are the battery temperature at the time of 0 and t, T_{amb} is the ambient temperature, ρ_b is the density of the battery, c_b is the specific heat of the battery, V_b is the volume of the battery.

Under different charge-discharge rates and ambient temperatures conditions, the heat generation rate at a given time could be determined according to Eq. (1) and the related battery temperature drop data show in the literature [35]. In order to conveniently using the heat generation rate in simulations, the following polynomial expressions for the cases of 4C rate of charge and discharge, as well as 35 ^{o}C and 42 ^{o}C were fitted by utilizing the least square method.

$$q = a_0 + a_1 t + a_2 t^2 + \cdots + a_n t^n \ , n = 1, 2, \cdots, t \le t_{total} \tag{2}$$

where a_0, a_1, $\cdots$, a_n are constant for a given charge-discharge rate and ambient temperature.

When n was equal to 7, the polynomial fitting R-square was more than 0.988. This indicated that the curve was matching well with the calculation value of the heat generation. Table 2 shows the coefficient of the polynomial fitting for the cases of 4C charge and discharge at 35 ^{o}C and 4C discharge at 42 ^{o}C.

Table 2. Coefficient of polynomial fitting at 4C charge and discharge at 35 ^{o}C and 42 ^{o}C

Condition	a_0	a_1	a_2	a_3	a_4	a_5	a_6	a_7
4C dis-35	-3.7375	0.6863	-0.0133	1.1742E-4	-5.6878E-7	1.6347E-9	-2.8544E-12	2.9673E-15
4C charg-35	0.1119	0.3846	-0.0071	5.1582E-5	-2.8953E-10	7.8784E-10	-1.2799E-12	1.2271E-15
4C dis-42	-1.6505	0.5777	-0.0123	1.1533E-4	-5.8328E-7	1.7314E-9	-3.0989E-12	3.2834E-15

The polynomial expressions under different conditions were implemented with coupling the solutions of the governing equations via a user defined function in ANYSYS Fluent 14.0. The calculation of the heat generation rate provided the heat source for each battery cell.

The standard governing equations of continuity, momentum and energy equation were used for the fluid domain. While only the energy conservation equation was used for both battery cell domain and PCM domain.

Based on energy conservation and the assumptions in section 3.2, for the domain of the cells, the energy equation can be defined by Eq. (3):

$$\rho_{\mathrm{b}} c_{\mathrm{b}} \frac{\partial T}{\partial t} = \nabla \cdot \left(k_{\mathrm{b}} \nabla T\right) + q_{\mathrm{dot}} \tag{3}$$

where k_b is the thermal conductivity of the battery, q_dot is the battery cell heat generation rate per unit volume.

For the domain of the PCM, since a pure heat conduction process was considered as the PCM was melting or solidifying, the energy equation can be calculated as follows:

$$\rho_{\mathrm{p}} \frac{\partial H}{\partial t} = \nabla \cdot \left(k_{\mathrm{p}} \nabla T\right) \tag{4}$$

$$H = \int_{T_{\mathrm{ref}}}^{T} c_{\mathrm{p}} dT + \beta L \tag{5}$$

where ρ_p is the density of the PCM, H is the enthalpy of the PCM, k_b is the effective thermal conductivity of the PCM, L is the latent heat of the PCM, β is the liquid fraction of the PCM, which can be expressed as [25]:

$$\beta = \begin{cases} 0 & T < T_{\mathrm{s}} \\ \left(T - T_{\mathrm{s}}\right) / \left(T_{\mathrm{l}} - T_{\mathrm{s}}\right) & T_{\mathrm{s}} < T < T_{\mathrm{l}} \\ 1 & T > T_{\mathrm{l}} \end{cases} \tag{6}$$

where T_s and T_l are the solidification and liquefaction temperature of the PCM, respectively.

For the domain of the fluid (air), the continuity, momentum and energy equations were given by Eqs. (7), (8) and (9), respectively.

$$\frac{\partial \rho_{\mathrm{f}}}{\partial t} + \nabla \cdot \left(\rho_{\mathrm{f}} \vec{u}\right) = 0 \tag{7}$$

$$\frac{\partial \left(\rho_{\mathrm{f}} \vec{u}\right)}{\partial t} + \nabla \cdot \left(\rho_{\mathrm{f}} \vec{u} \vec{u}\right) = -\nabla p_{\mathrm{f}} + \nabla \cdot \left(\mu_{\mathrm{f}} \nabla \vec{u} + \mu_{\mathrm{f}} \nabla \vec{u}^{\mathrm{T}}\right) \tag{8}$$

$$\frac{\partial \left(\rho_{\mathrm{f}} c_{\mathrm{f}} T\right)}{\partial t} + \nabla \cdot \left(\rho_{\mathrm{f}} c_{\mathrm{f}} \vec{u} T\right) = \nabla \cdot \left(k_{\mathrm{f}} \nabla T\right) \tag{9}$$

where ρ_f and c_f are the density and specific heat of the cooling air, $\vec{u}$ is the velocity vector of the cooling air, μ_f is the dynamic viscosity of the cooling air and p_f is the static pressure. Besides, the turbulent model, k-ε model, was employed to predict the flow behavior [36].

3.3. Model validation

In the simulation, the numerical model for describing the PCM melting and the heat generation of the battery are crucial for the simulation results. The following section shows the comparison of the simulation and experimental results to validate the numerical model.

3.3.1. Validation of PCM melting model

In order to validate the melting model of the PCM, the experimental test using an electric heater instead of the actual cell was carried out at 35 ^{o}C (ambient temperature). The heat power was constant and set to 5 W. The test section, as shown in Fig. 2, was placed in the thermostat chamber and the natural convection heat transfer coefficient was estimated to 5 W/m^2·K. The temperature of the same location on the surface of the battery and PCSEUs under experimental and simulating conditions was selected for comparison. Fig. 5 depicts the comparison of the simulated and experimental surface temperatures for the battery, PCSEU-1 and PCSEU-2.

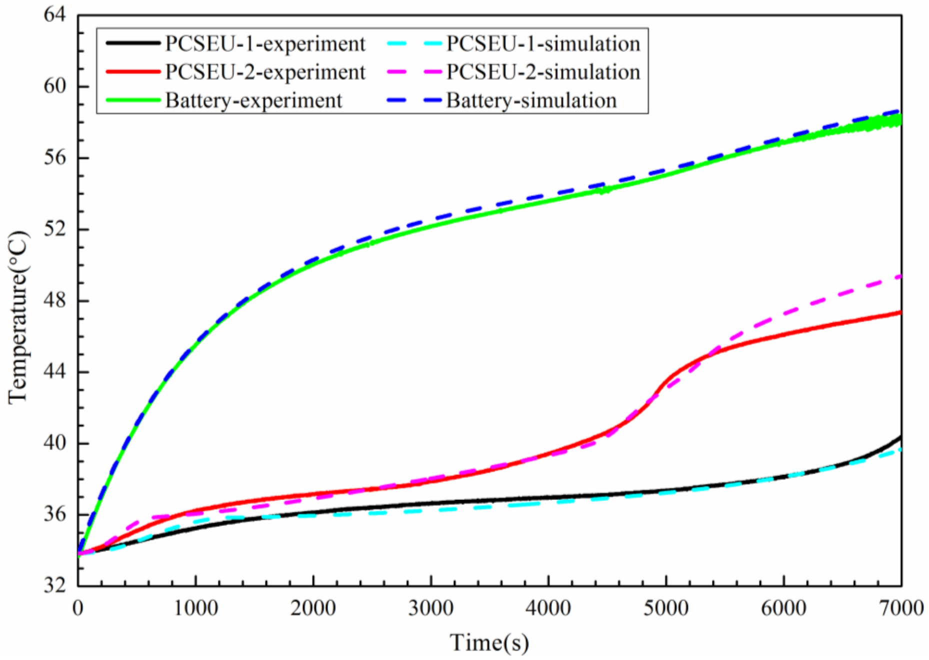

Fig. 5. The experimental and simulation results of the battery and PCSEUs.

It can be clearly seen from Fig. 5 that there were the similar change trends of the battery and PCSEUs temperatures under both simulation and experiment conditions. Good agreements were achieved between the experimental data and the computed results. Overall, the maximum error was not more than 5%.

3.3.2. Validation of battery heat generation rate

For the purpose of verifying the heat generation rate of the battery, the experiment and simulation on the thermal behavior of the ITMS were carried out at 4C charge and discharge rates under natural convection conditions. The ambient temperature was 35 °C. The comparison of battery temperature between experimental data and simulated results is presented in Fig. 6.

As shown in Fig. 6, it could be found that the simulated temperature was in good agreement with experimental one. The maximum error was 2.1% during 4C charge process whereas 1.3% during 4C discharge process. The result demonstrated that the heat generation rate model was robust and accuracy.

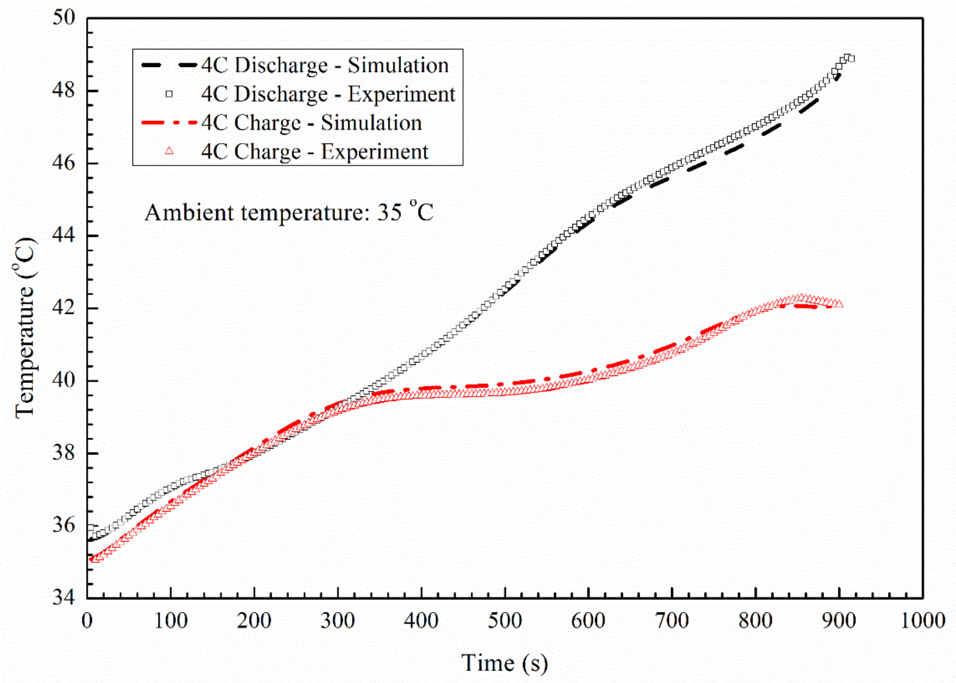

Fig. 6. The simulation and experimental battery temperatures at 4C charge-discharge rates.

4. Results and discussion

The results are presented in the following four sections. The first section analyzes the effect of the air flow rate and PCM liquid fraction on the thermal behavior of the ITMS. The second describes the performance difference between the ITMS and the ACS. The third and fourth sections will look at the thermal characteristics of the ITMS and ACS during charge-discharge cycles.

4.1. Thermal behavior of the ITMS

It needs to be emphasized that the battery temperature can be affected by both the cooling air flow rate and the liquid fraction of the PCM.

4.1.1. Effect of air flow rate

Fig. 7 shows the maximum temperature variation of the battery pack with the ITMS under 4C charge-discharge rate at ambient temperature of 42 °C. The air flow rate is 7 m^3/h and 18 m^3/h, respectively. The temperature profiles during the period of air cooling are interrupted since the charge and discharge are not carried out continuously. It can be clearly seen from Fig. 7 that increasing air flow rate leads to the decrease of the battery temperature. Due to insufficient cooling after discharge, the initial temperature of the battery at the beginning of charge becomes higher than that before discharge. Furthermore, higher initial temperature of the battery plays a negative role in reducing the battery temperature.

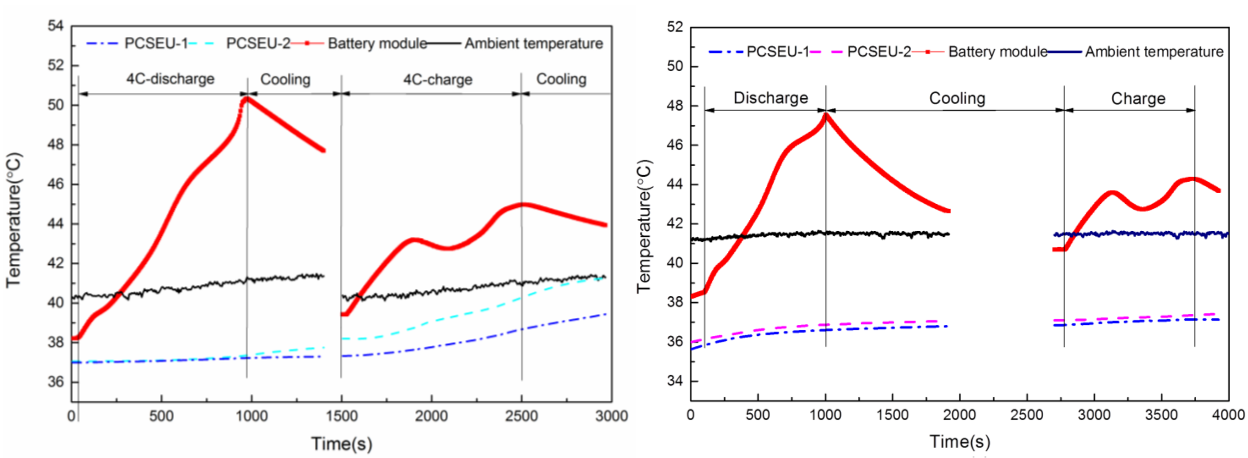

(a) 42 °C-7 m^3/h (b) 42 °C-18 m^3/h

Fig. 7 Temperature change of battery during 4C discharge and charge process under different conditions: (a) 42 °C-7 m^3/h; (b) 42 °C-18 m^3/h.

In Fig. 7(a), the battery temperature increases continuously during the 4C discharge process and reaches the highest value of 50.3 °C at the end of 4C discharge when the air flow rate is 7 m^3/h. The maximum temperature rise is 12 °C. The surface temperatures of the PCSEU-1 and PCSEU-2 are approximately 37.0 °C during the whole discharge. This indicates that the heat generated by the battery is stored in latent heat. After the 4C discharge process, air cooling with the flow rate of 40 m^3/h is used and the battery temperature drops rapidly. The temperatures of the PCSEU-1 and PCSEU-2 slightly increase since the battery temperature is higher than the phase change temperature. In the 4C charge process, the initial temperature of the battery is 39.5 °C and the temperature curve has two peaks. Both peak values are 43.2 °C and 44.8 °C, respectively. The temperature drop during the intermediate period is the consequence of the domination of the heat dissipation against the battery heat generation. The PCM in the PCSEU-1 fully melts firstly and then that in the PCSEU-2 does in terms of their temperature. The highest temperature of the battery is very close to the upper limit temperature of 45 ^{o}C.

As illustrated in Fig. 7(b), when the air flow rate is 18 m^3/h, the highest temperature of the battery reaches 47.7 ^{o}C with the maximum temperature rise of 9.3 ^{o}C at the end of the 4C discharge process. This implies that increasing air flow rate can decline the battery highest temperature. The temperatures of the PCSEU-1 and PCSEU-2 are close to 37.0 ^{o}C, which means that part of PCM melts. For the case of 4C charge, the initial temperature is 40.6 ^{o}C. The highest temperature of the battery gets to 44.2 ^{o}C under the coupled action of the cooling air and the PCMs. There are also two temperature peaks with very small temperature difference. Compared with the temperature curves of the 4C charge process under 7 m^3/h and 18 m^3/h conditions, the temperature difference between both peaks is 1.8 ^{o}C as the air flow rate is 7 m^3/h. While at 18 m^3/h, the temperature difference is only 0.6 ^{o}C. Therefore, the increase of air flow rate could reduce the temperature fluctuation of the battery during the charge period and improve the battery temperature stability level.

4.1.2. Effect of PCM liquid fraction

Because the phase change cooling of the PCM depends essentially on the storage of the heat generated by the battery, the liquid fraction of the PCM is a significant index denoting the phase change progress and effectiveness of the PCM itself. It can be estimated in accordance with the surface temperature of the PCSEUs. When the surface temperature is below 36 ^{o}C, the PCMs inside the PCSEUs do not melt and the liquid fraction is equal to 0 (β=0). When the surface temperature is above 36.0 ^{o}C and below 38.0 ^{o}C, the solid and liquid PCMs coexist, namely, 0<β<1. When the temperature exceeds 38.0 ^{o}C, the PCM entirely melts and β=1.

Fig. 8 presents the temperature profiles of the battery and PCSEUs at 35 ^{o}C and 42 ^{o}C at different liquid fractions. The air flow rate is 7 m^3/h and 24 m^3/h, respectively. The charge and discharge rate is 4C. From Fig. 8(d) to Fig. 8(f), since the charge-discharge cycles are not conducted continuously, the temperature curves are interrupted during the cooling process. It can be found in Fig. 8 that for a fixed ambient temperature and air flow rate, different liquid fractions would not result in a significant change of the battery temperature. The battery temperature does not appear sharp rise even after the PCM fully melts.

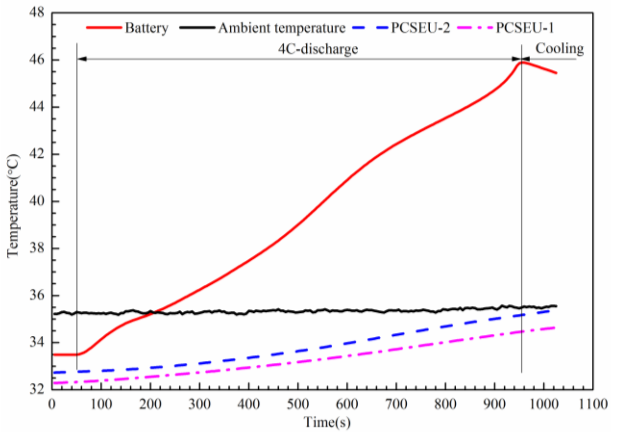

(a) 7 m^3/h-35 ^{o}C, β=0

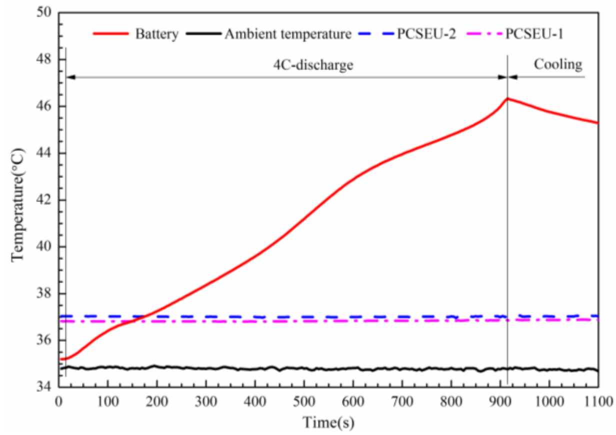

(b) 7 m^3/h-35 ^{o}C, 0<β<1

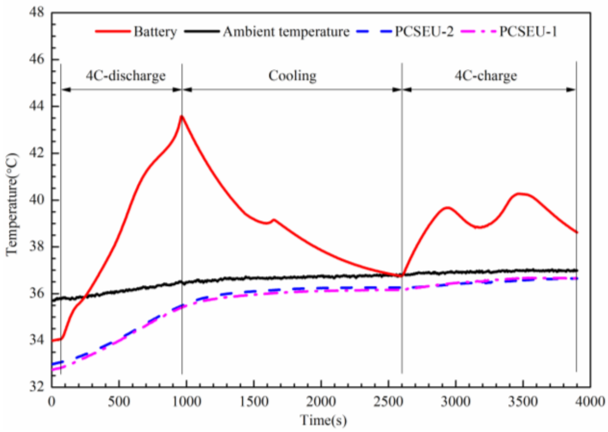

(c) 24 m^3/h-35 ^{o}C, β=0

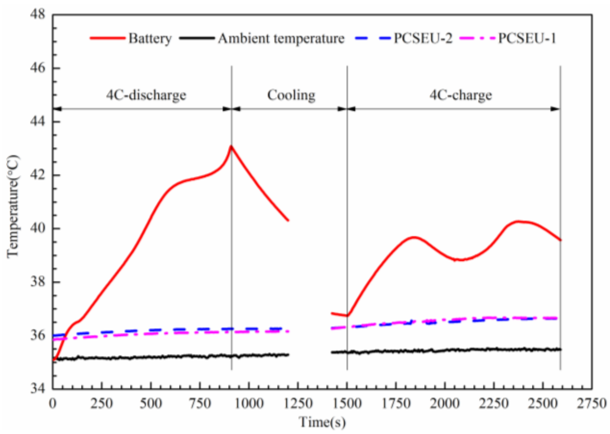

(d) 24 m^3/h-35 ^{o}C, 0<β<1

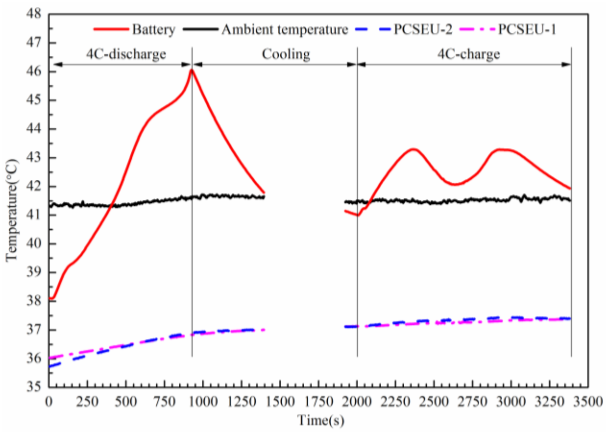

(e) 24 m^3/h-42 ^{o}C, 0<β<1

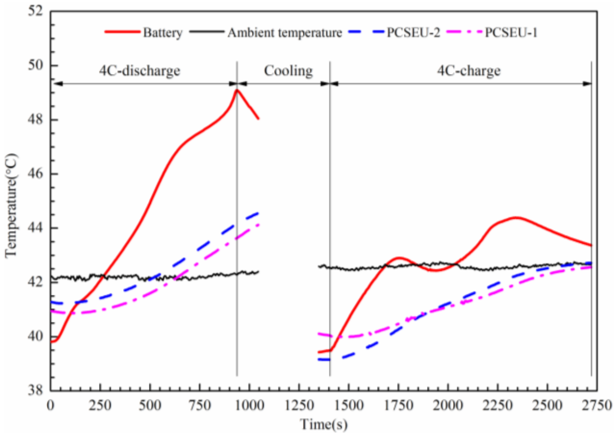

(f) 24 m^3/h-42 ^{o}C, β=1

Fig.8. The battery temperature of ITMS under different liquid fractions conditions. (a) 7 m^3/h-35 ^{o}C, β=0; (b) 7 m^3/h-35 ^{o}C, 0<β<1; (c) 24 m^3/h-35 ^{o}C, β=0; (d) 24 m^3/h-35 ^{o}C, 0<β<1; (e) 24 m^3/h-42 ^{o}C, 0<β<1; (f) 24 m^3/h-42 ^{o}C, β=1

In Fig. 8(a), during the entire 4C discharge process, the temperatures of the PCSEUs increase slowly and are always below the melting point. This means that the PCMs inside the PCSEUs do not melt. Some of the heat generated by the battery is absorbed by the heat capacity of the cell and the other part is mainly dissipated by the cooling air. The highest temperature of the battery is 46.2 ^{o}C and the temperature rise is 12.7 ^{o}C at the end of the discharge. As shown in Fig. 8(b), the temperatures of the PCSEUs are nearly close to 37 ^{o}C, which indicates that the PCMs partially melt. The highest temperature of the battery is 46.3 ^{o}C with the temperature rise of 11.1 ^{o}C as the discharge ends. In comparison, it is obvious that the heat absorption of the PCMs in Fig. 8(a) is less than that in Fig. 8(b). Additionally, the higher initial temperature of the battery causes the larger battery temperature.

During the entire charge and discharge process illustrated in Fig. 8(c), the PCMs inside the PCSEUs are always in solid state. The cooling air dissipated most of the heat from the battery. A small amount of the heat was stored in the PCMs in the form of sensible heat. Consequently, the highest temperature of the battery was 43.5 ^{o}C and 40.4 ^{o}C at the end of the 4C discharge and charge, respectively. The temperature rise during discharge and charge was 9.5 ^{o}C and 3.7 ^{o}C, respectively. For the case shown in Fig. 8(d), part of the PCMs melts in terms of the temperatures of the PCSEUs. The highest temperature of the battery is 43.1 ^{o}C and 40.1 ^{o}C, respectively. The temperature rise in discharge and charge process is 8.1 ^{o}C and 3.3 ^{o}C, respectively.

Furthermore, it can be clearly seen from Fig. 8(a) to Fig. 8(d) that, increasing air flow rate from 7 m^3/h to 24 m^3/h, the heat dissipation ratio of the air cooling increases and the battery temperature descends. For the case of airflow rate of 24 m^3/h at 35 ^{o}C, the highest temperature of the battery is nearly close under β=0 and 0<β<1 conditions. This may be resulted from the lower initial temperature of the battery as β=0.

In Fig. 8(e), the highest temperature of the battery is 46.1 ^{o}C and the temperature rise is 8.0 ^{o}C during the 4C discharge period. Compared with the case of 4C discharge shown in Fig. 8(c), there is almost the same temperature rise. In the next 4C charge process, the highest temperature of the battery is 43.3 ^{o}C and the temperature rise is 2.3 ^{o}C.

As demonstrated in Fig. 8(f), the highest temperature of the battery reaches 49.3 ^{o}C and the temperature rise is 9.5 ^{o}C during the 4C discharge period. The temperatures of the PCSEU-1 and PCSEU-2 exceed 41 ^{o}C and rose rapidly, which infers PCMs full melting. The PCMs store the heat in sensible heat. During the 4C charge process, the highest temperature of the battery is 44.3 ^{o}C with the temperature rise of 5 ^{o}C. For the two peaks on the temperature curve, the second peak value is significantly higher than the first peak. This indicates that PCM entire melting could enlarge the battery temperature fluctuation during the charge period and worsen the temperature stability. In contrast to the result shown in Fig. 8(e), the highest temperature of the battery under 4C discharge conditions magnifies 3.2 ^{o}C and there is a higher temperature rise for 4C charge process. However, It can be recognized that the battery temperature does not ascend rapidly even the PCMs fully melts. The main reason can be explained as follows. Due to the short time of single charge or discharge, the effect of the PCM complete melting has not yet been fully acted. On the other hand, the parallel arrangement of the PCSEU-1 and PCSEU-2 in the ITMS does not cause a very notable change of thermal resistance between the battery cell and PCMs. Besides, the PCSEUs do not have a negative influence on the air cooling and the majority of the heat is removed by the cooling air.

4.2. Comparison of thermal behavior of ITMS and ACS

In order to further study the effects of ambient temperature and air flow rate on the thermal performance of the ITMS, the maximum temperature and temperature difference of the battery pack with the ITMS and ACS are depicted in Fig. 9. The ambient temperature is 35 ^{o}C and 42 ^{o}C and the air flow rate is 7 m^3/h, 18 m^3/h and 24 m^3/h, respectively. The discharge rate is 4C. For the ACS, since the battery temperature exceeds the safety temperature of 55 ^{o}C under 42 ^{o}C and 7 m^3/h conditions, the corresponding temperature in Fig. 9 is set to 55 ^{o}C under this condition.

As illustrated in Fig. 9(a), the maximum temperature of the battery pack for the ITMS at 35 ^{o}C and 42 ^{o}C is 46 ^{o}C and 50.3 ^{o}C, respectively. They are less than those for the ACS under the same conditions. When the air flow rate reduces from 24 m^3/h to 7 m^3/h, the battery temperature at 35 ^{o}C and 42 ^{o}C increases 3.1 ^{o}C and 4.3 ^{o}C, respectively. The temperature rise is smaller than that for the ACS under the fixed ambient temperature. This indicates that the effect of the air flow rate change on the battery temperature for the ITMS is not significant relative to that for the ACS. This is due to the heat dissipation only by air cooling in the ACS. Thus, the change of the air flow rate obviously alerts the battery temperature. But in the ITMS, both air cooling and phase change cooling are contributed to the heat dissipation. Changing the air flow rate mainly affects the heat dissipation of air cooling rather than the phase change cooling.

For the ACS, increasing ambient temperature does not lead to an apparent decrease of the battery temperature rise, but significantly increases the battery temperature. For the ITMS, however, as the ambient temperature is 35 °C, the battery temperature rise is 11.4 °C, 9.0 °C and 8.2 °C at the flow rate of 7 m^3/h, 18 m^3/h and 24 m^3/h, respectively. While the ambient temperature is 42 °C, the temperature rise is 8.2 °C, 5.5 °C and 4.2 °C, respectively. The increase of the ambient temperature from 35 °C to 42 °C obviously reduces the battery temperature rise. Simultaneously, the battery temperature increases 3.7 °C, 3.5 °C and 3.0 °C, respectively. Consequently, the influence of the ambient temperature change on the battery temperature rise for the ITMS is obviously less than that of the ACS. The main reason could be that the variation of the ambient temperature significantly changes the heat dissipation of the air cooling, but almost not change the heat absorption of the PCMs.

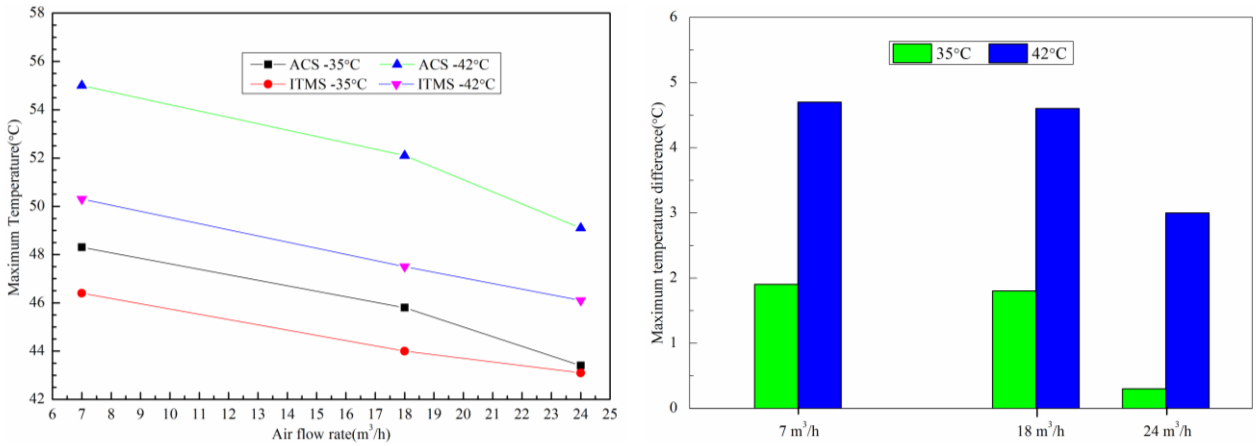

(a) The maximum temperature （b）The maximum temperature difference

Fig. 9. The temperature of the battery pack for the ITMS and ACS. (a) The maximum temperature of the battery (b) The maximum temperature difference.

From the bar graph of the maximum temperature difference between the ITMS and ACS shown in Fig. 9(b), it can be clearly seen that the temperature difference decreases with the air flow rate increasing at a fixed ambient temperature. The lower the ambient temperature, the smaller the temperature difference. For the case of 7 m^3/h, the temperature difference is 1.9 °C at 35 °C but is 4.6 °C at 42 °C. When the air flow rate is 24 m^3/h, the temperature difference is only 0.3 °C at 35 °C and 3 °C at 42 °C. The great temperature difference shows that the cooling effect of the ITMS is better than that of the ACS. For a fixed ambient temperature, the cooling effect distinction between the ITMS and ACS is small at a large air flow rate. For a fixed flow rate, the cooling effect of the ITMS is better than that of the ACS at a larger ambient temperature. The main reason for the result is that the heat dissipation ratio of the PCMs and the total heat generation is different at different ambient temperatures and air flow rates. When the ratio is higher, the battery temperature is lower.

4.3. Thermal behavior of ACS during charge-discharge cycle

This section presents the thermal behavior of the ACS for the entire battery pack during single 4C discharge and charge-discharge cycle. In the current simulations, the ambient temperature is set to 35 ^oC and 42 ^oC, respectively. The air flow rate in the range from 50 m^3/h to 500 m^3/h is used. The initial temperature of the battery pack is equal to ambient temperature.

4.3.1. Thermal behavior of ACS during single 4C discharge

Under different air flow rates and ambient temperatures conditions, the maximum and minimum values of the air flow velocity and the battery temperature are illustrated in Table 3. It can be clearly seen from Table 3 that the larger air flow rate causes the larger air velocity flowing through the battery surface and the lower battery temperature. When the air flow rate is 50 m^3/h, the maximum temperature of the battery is 49.3 ^oC at 35 ^oC, which is in the safe temperature range. While the maximum temperature reaches 55.9 ^oC at 42 ^oC, which exceeds the upper limit of the safe range. For the case of 100 m^3/h and 42 ^oC, the battery is at more risk of overheating owing to the maximum temperature of 54.8 ^oC. At a small air flow rate, the difference between the maximum and minimum velocity is also small. However, the velocity difference enlarges with the increase of the air flow rate.

Table 3. The velocity and temperature at different flow rates and ambient temperatures.

Q	u_{min}	u_{max}	ΔP	T_a=35 ^oC			T_a=42 ^oC		
/m^3/h	/m/s	/m/s	/Pa	T_{max}/ ^oC	T_{min}/ ^oC	ΔT/ ^oC	T_{max}/ ^oC	T_{min}/ ^oC	ΔT/ ^oC
50	1.3	1.5	54	49.3	49.1	0.2	55.9	55.7	0.2
100	2.4	3.3	127	48.1	47.2	0.9	54.8	53.9	0.9
150	3.4	5.1	243	47.1	45.7	1.4	53.8	52.4	1.4
200	4.5	6.9	380	46.2	44.4	1.7	52.9	51.2	1.7
300	6.6	10.4	781	44.6	42.5	2.1	51.4	49.3	2.1
400	8.7	14.0	1326	43.3	41.0	2.4	50.1	47.8	2.3
500	10.8	17.5	2009	42.3	39.4	2.9	49.1	46.3	2.8

The non-uniform distribution of the flow field leads to the temperature difference of the battery. Moreover, the higher the air flow rate, the higher the temperature difference. Due to the arrangement in parallel of the battery modules inside the battery box, the great velocity difference under large flow rate conditions does not cause a great temperature difference during single 4C discharge mode. For example, the difference between the maximum and minimum velocity at 500 m^3/h is 6.7 m/s. The relative temperature difference at 35 ^oC and 42 ^oC is 2.9 ^oC and 2.8 ^oC, respectively. In addition, the pressure difference increases rapidly with the increase of the air flow rate. The high pressure difference requires the large power fan to drive the air flowing.

4.3.2. Thermal behavior of ACS during charge-discharge cycle

In the actual application, the battery operates with many charge-discharge cycles. In order to investigate the thermal behavior of the ACS during charge-discharge cycle, numerical simulations are carried out for two 4C charge-discharge cycles. Fig. 10 depicts the maximum temperature and temperature difference profiles of the entire battery pack at the ambient temperature of 35 ^oC. The battery pack is cooled by the forced convection between the charge and discharge process and the cooling time is set to 10 minutes.

In Fig. 10(a), for the case of 100 m^3/h and 35 ^oC, the maximum temperature of the battery pack is 49.5 ^oC during the first charge-discharge cycle. However, during the second 4C discharge process, the maximum temperature of the battery reaches 56 ^oC, which exceeds the upper limit of the safe range. As the flow rate increases to 200 m^3/h, although the battery temperature is in the safe range during two cycles, the battery temperature reaches 49.0 ^oC at the end of the second 4C discharge and the temperature rise is 14.0 ^oC. It can also be found that the battery is not able to be cooled enough before the beginning of the second cycle under the case of 100 m^3/h and 200 m^3/h.

For the case of 42 ^oC and 200 m^3/h, the battery temperature also exceeds the safety temperature, which is not shown in Fig. 10(a). When the air flow rate increases to 300 m^3/h, the battery temperatures are nearly the same under both charge-discharge cycles conditions. The maximum temperature of the battery pack is 45.1 ^oC. The reason is that the large air flow rate can provide enough cooling for the battery pack and induce a low initial temperature of the battery at the start of the next charge or discharge. This also indicates that the improvement of the thermal behavior of the ACS relies on the initial temperature during the charge-discharge cycle period since the battery temperature is in the safe range in a single cycle.

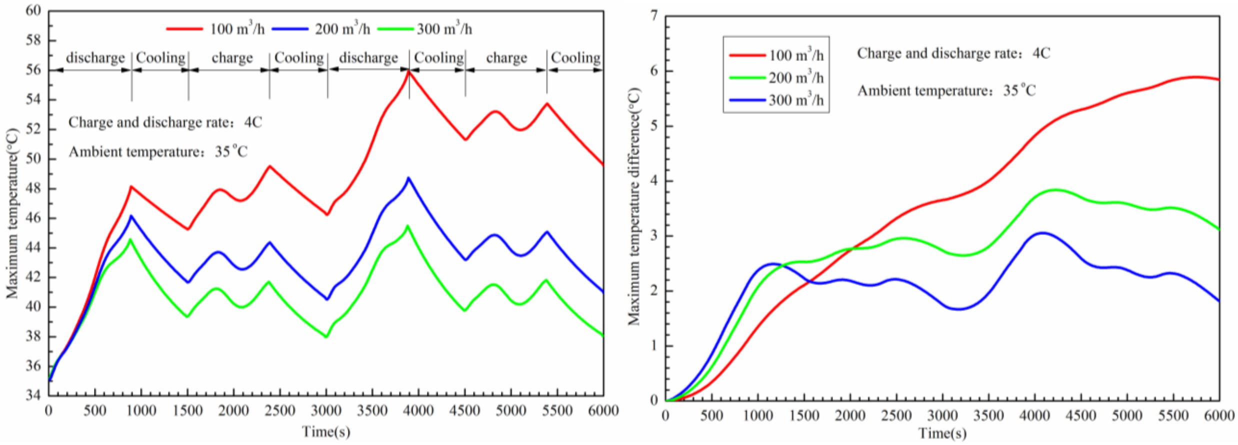

(a) Battery maximum temperature (b) Maximum temperature difference

Fig. 10. Temperature profiles of the entire battery pack during two 4C charge-discharge cycles. (a) Battery maximum temperature. (b) Maximum temperature difference.

According to Eq. (1), assuming that the internal thermal resistance of the battery is neglected, when q=0 the relationship between the battery temperature drop and the cooling time and air flow rate is as follows.

$$T = (T_0 - T_{\mathrm{amb}})\exp\left(-\frac{hA}{\rho_{\mathrm{b}} c_{\mathrm{b}} V_{\mathrm{b}}} t\right) + T_{\mathrm{amb}} \quad (10)$$

It can be obtained from Eq. (10) that increasing the cooling time or the air flow rate in the same proportion could enlarge the temperature drop of the battery. Moreover, the temperature drops are nearly the same.

As can be seen from Fig. 10(b), the maximum temperature difference of the battery pack shows a general rise trend with the increase in the number of cycles under different air flow rates conditions. During the discharge, the temperature difference ascends rapidly. When the air flow rate is 100 m^3/h, the temperature difference ascends continuously during the whole cycles and the maximum value gets to 5.9 ^{o}C. While at 200 m^3/h, the temperature difference ascends during the first charge but descends during the second charge. It also descends in the second cooling stage and second discharge initial stage. The maximum temperature difference is 3.8 ^{o}C after the second discharge ends. When the air flow rate is 300 m^3/h, the temperature difference change is similar with that at 200 m^3/h during the entire cycles except for the first charge. The maximum temperature difference is 3.1 ^{o}C. Unlike the temperature difference increasing with the increase of the air flow rate in a single discharge mode, as shown in Table 3, the maximum temperature difference during the charge-discharge cycle is larger when the air flow rate is smaller.

Based on the above analyses, the air flow rate cannot be below 300 m^3/h in order to meet the demand of the temperature control for the ACS. Furthermore, the greater the air flow rate, the better the cooling performance. However, increasing the air flow rate not only results in a poor temperature uniformity of the battery pack but also enlarges the pressure difference. Moreover, the large pressure difference significantly increases the power of the cooling fan. Thereby, a large amount of the battery power available is consumed. Obviously, the air cooling way will reduce the battery energy efficiency.

4.4. Thermal behavior of ITMS during charge-discharge cycle

For the battery pack with the ITMS, two different operation modes are presented. For the first operation mode, the PCMs are used as the only heat sink during the discharge period. Since there is external power, it can be used to drive the cooling fan without consuming the battery power. Consequently, both PCMs and cooling air are utilized to manage the battery temperature during the charge period. The cooling air flow rate is 300 m^3/h. Furthermore, the battery pack is cooled by the forced convection after the charge and discharge finish. In the second mode, the ITMS works during the charge and discharge cycles. The air flow rate is 100 m^3/h. The cooling time after charge and discharge is set to 10 minutes for the above two modes.

The temperature profiles of the whole battery pack during 4C charge-discharge cycles are demonstrated in Fig. 11. It should be noted that at the end of the final cycle, the PCMs fully melts. It can be seen from Fig. 11 that the maximum temperature and the maximum temperature difference of the battery pack generally enlarge with the increase in the number of cycles. During each cycle, the battery temperature rises to the maximum value at the end of the discharge process and there are two temperature peaks in the charge process.

For the first operation mode, as shown in Fig. 11(a), the maximum temperature of the battery pack gets to 49.2 ^oC. Due to the large cooling air flow rate, the battery temperature in the cooling process drops rapidly under forced convection cooling. The initial temperature of the battery in the next cycle is reduced effectively. Moreover, the temperature difference between both peaks during the charge process becomes bigger with the charge-discharge cycle increasing. This operation mode reaches up to 6 charge-discharge cycles. During each cycle, the maximum temperature of the battery pack is 44.6 ^oC, 46.4 ^oC, 47.2 ^oC, 48.0 ^oC, 48.8 ^oC and 49.2 ^oC, respectively. In addition, the maximum temperature difference is 3.2 °C during all the cycles, which is less than the limited value. As the velocity distribution is not uniform, it is during the charge and cooling period that the temperature difference is large. In the 4C discharge process, the maximum temperature difference is only 1.5 °C, which is caused by the uneven initial temperature distribution.

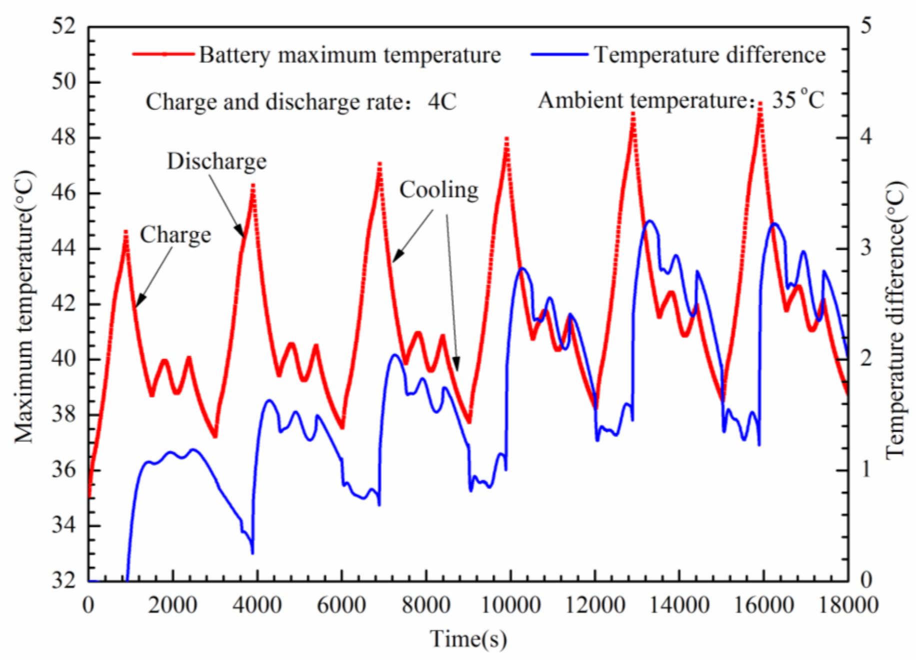

(a) The first operation mode

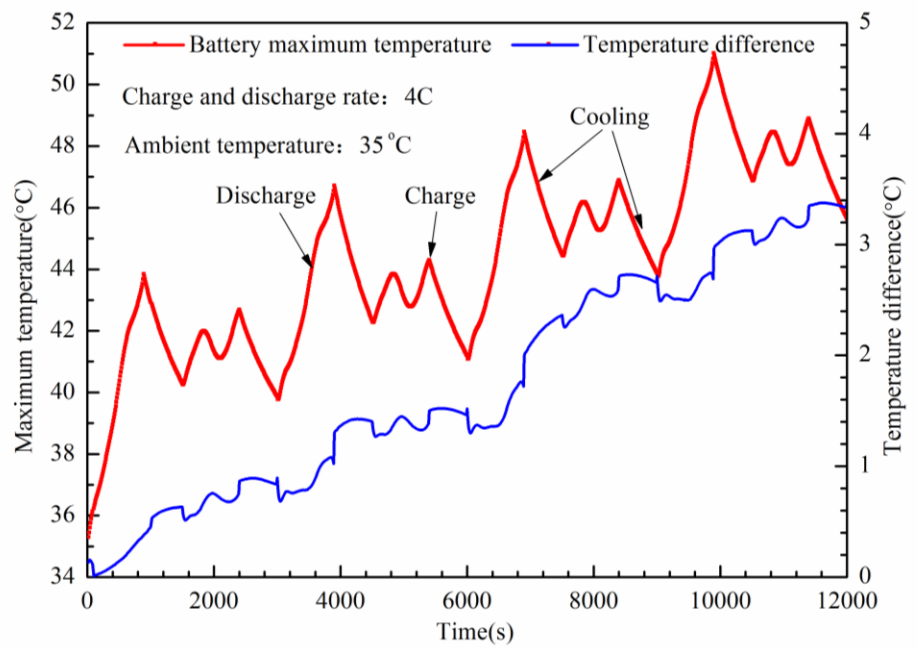

(b) The second operation mode

Fig. 11 Temperature profiles of battery pack during 4C charge-discharge cycle. (a) The first operation mode. (b) The second operation mode.

As illustrated in Fig. 11(b), up to 4 charge-discharge cycles are achieved and the maximum temperature of the battery pack reaches 51.0 ^{o}C. Because of the small air flow rate, the battery cannot be completely cooled after the completion of the charge and discharge and the initial temperature is large. As a consequence, the initial temperature in the next cycle increases. For the 4C charge process, the second peak temperature is higher than that of the first peak. During each cycle, the maximum temperature of the battery pack is 43.9 ^{o}C, 46.7 ^{o}C, 48.5 ^{o}C, and 51.0 ^{o}C, respectively. Furthermore, the maximum temperature difference is 3.3 ^{o}C. During the discharge process, the temperature difference increases generally, whereas during the cooling stage and charge process, the change of the temperature difference is small.

In order to better understand the temperature distribution of the battery pack, the temperature contours of local battery pack at a fixed time are depicted in Fig. 12. It is seen from Fig. 12 that the PCSEU-2 temperature is higher than the PCSEU-1 temperature and the temperature distributions of the battery cells are uniform for both operation modes. For the case shown in Fig. 12(a), the temperature of the battery cells at 18 000 s is lower than the PCSEU-2 temperature due to forced convection cooling. The temperature of the battery cells near the PCSEU-2 is higher than that at the other side. For the case shown in Fig. 12(b), the battery is charging at 8 100 s and the battery temperature is the greater than the PCSEUs temperature. The maximum temperature difference of the battery cells is less than 2.1 ^{o}C. The PCMs in the PCSEU-2 have melted completely and in the PCSEU-1 is melting.

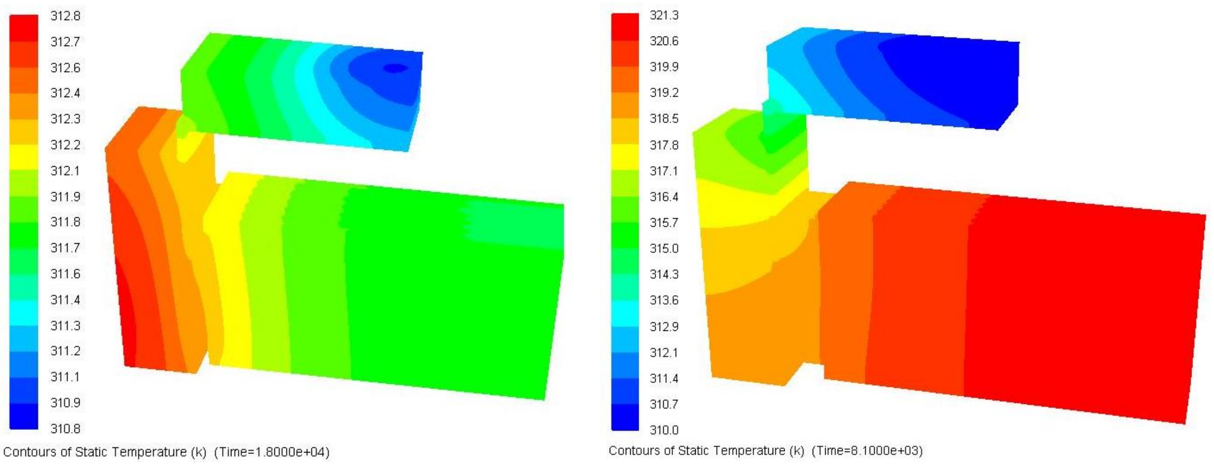

(a) The first operation mode (b) The second operation mode

Fig. 12 Temperature contours of local battery pack at fixed time. (a) The first operation mode. (b) The second operation mode.

As a result, for the first operation mode, the TMS is capable of effective controlling the battery temperature and does not need to consume the battery power. For the second operation mode, the TMS can also effectively control the battery temperature with a small air flow rate. But it needs to consume a certain amount of battery energy. Moreover, the maximum temperature of the battery pack is more than that of the first mode and the number of cycle is less than that of the first mode. In addition, it should be noted that both two operation modes can achieve infinite cycle if the enough cooling is provided after the charge and discharge finish.

5. Conclusions

A novel integrated thermal management system by integrating air cooling and PCM was proposed for the lithium-ion power battery pack. The thermal behavior of the ITMS was studied both experimentally and numerically to verify the effectiveness of the thermal management and the accuracy of the simulation model. The impact factors including the air flow rate, ambient temperature and PCM liquid fraction were taken into account. Moreover, the charge-discharge cycle characteristics were simulated for the entire battery pack with both ITMS and ACS. The main conclusions are given as follows:

(1) The overheating of the battery with the ACS occurred at 42 ^{o}C and 4C discharge as the air flow rate was less than 7 m^3/h. However, the temperature of the battery with the ITMS could be sustained within 55 ^{o}C even under 7 m^3/h and 42 ^{o}C conditions.

(2) The variations of the air flow rate and ambient temperature mainly affected the heat removal of the air cooling instead of the phase change cooling. For the cases where the PCM did not melt and partially melted, the battery maximum temperatures showed a small difference. Even as the PCMs fully melted, the battery temperature did not significantly rise due to the effect of air cooling.

(3) Decreasing the battery initial temperature during charge-discharge cycles was crucial to improve the cycle thermal characteristics of the ITMS. The ACS with air flow rate exceeding 300 m^3/h could meet the demands of the battery thermal management. But it significantly consumed more battery power and led to much higher temperature difference.

(4) For both operation modes of the ITMS, the first mode without consumption of the battery power could effectively control the battery temperature below 49.2 ^{o}C and the temperature

difference within 3.2 °C during up to six 4C charge-discharge cycles. While the second mode with air flow rate of 100 m^3/h just reached up to four cycles although it could manage the battery temperature below 51.0 °C and the temperature difference within 3.3 °C during 4C cycles.

Acknowledgement

The authors would like to acknowledge the financial support from University of Hertfordshire, United Kingdom. This work was supported by the CRRC TANGSHAN CO., LTD.

References

[1] Malik M, Dincer I, Rosen MA. Review on use of phase change materials in battery thermal management for electric and hybrid electric vehicles. International Journal of Energy Research, 2016, 40(8): 1011-1031.

[2] Liu H, Wei Z, He W, Zhao J. Thermal issues about Li-ion batteries and recent progress in battery thermal management systems: A review. Energy Conversion and Management, 2017, 150: 304-330.

[3] Madani SS, Swierczynski MJ, Kær SK. A review of thermal management and safety for lithium ion batteries. Ecological Vehicles and Renewable Energies (EVER), 2017 Twelfth International Conference on. IEEE, 2017: 1-20.

[4] Lu L, Han X, Li J, Hua J, Ouyang M. A review on the key issues for lithium-ion battery management in electric vehicles. Journal of power sources, 2013, 226: 272-288.

[5] Fan L, Khodadadi JM, Pesaran AA. A parametric study on thermal management of an air-cooled lithium-ion battery module for plug-in hybrid electric vehicles. Journal of Power Sources, 2013, 238: 301-312.

[6] Panchal S, Khasow R, Dincer I, Agelin-Chaab M, Frasera R, Fowlerc M. Thermal design and simulation of mini-channel cold plate for water cooled large sized prismatic lithium-ion battery. Applied Thermal Engineering, 2017, 122: 80-90.

[7] Rao Z, Wang S, Zhang G. Simulation and experiment of thermal energy management with phase change material for ageing $LiFePO_4$, power battery. Energy Conversion and Management, 2011, 52(12): 3408-3414.

[8] Putra N, Ariantara B, Pamungkas RA. Experimental investigation on performance of lithium-ion battery thermal management system using flat plate loop heat pipe for electric vehicle application. Applied Thermal Engineering, 2016, 99: 784–789.

[9] Wu MS, Liu KH, Wang YY, Wan CC. Heat dissipation design for lithium-ion batteries. Journal of Power Sources, 2002, 109(1): 160-166.

[10] Park S, Jung D. Battery cell arrangement and heat transfer fluid effects on the parasitic power consumption and the cell temperature distribution in a hybrid electric vehicle. Journal of Power Sources, 2013, 227(4): 191-198.

[11] Sabbah Rami，Kizilel R，Selman J R， Al-Hallaj S. Active（air-cooled）vs，passive（PCM）thermal management of high-power Li-ion packs: Limitation of temperature rise and uniformity of temperature distribution. Journal of Power Sources, 2008, 182: 630-638.

[12] Chen D, Jiang J, Kim G H, Yang C, Pesaran A. Comparison of different cooling methods for lithium ion battery cells. Applied Thermal Engineering, 2016, 94: 846-854.

[13] De Vita A, Maheshwari A, Destro M, Santarelli M, Carello M. Transient thermal analysis of a lithium-ion battery pack comparing different cooling solutions for automotive applications. Applied Energy, 2017, 206: 101-112.

[14] Huo Y, Rao Z, Liu X, Zhao J. Investigation of power battery thermal management by using mini-channel cold plate. Energy Conversion and Management, 2015, 89: 387-395

[15] Zhao J, Rao Z, Li Y. Thermal performance of mini-channel liquid cooled cylinder based battery thermal management for cylindrical lithium-ion power battery. Energy Conversion and Management, 2015, 103: 157-165.

[16] Qian Z, Li Y, Rao Z. Thermal performance of lithium-ion battery thermal management system by using mini-channel cooling. Energy Conversion and Management, 2016, 126: 622-631.

[17] Farid MM, Khudhair AM, Razack SAK, Al-Hallaj S. A review on phase change energy storage: materials and applications. Energy conversion and management, 2004, 45(9): 1597-1615.

[18] Lv Y, Yang X, Li X, Zhang G, Wang Z, Yang C. Experimental study on a novel battery thermal management technology based on low density polyethylene-enhanced composite phase change materials coupled with low fins. Applied Energy, 2016, 178: 376-382.

[19] Al-Hallaj S, Selman JR. A Novel Thermal Management System for Electric Vehicle Batteries Using Phase‐Change Material. Journal of the Electrochemical Society, 2000, 147(9): 3231-3236.

[20] Al-Hallaj S, Selman JR. Thermal modeling of secondary lithium batteries for electric vehicle/hybrid electric vehicle applications. Journal of power sources, 2002, 110(2): 341- 348.

[21] Ling Z, Zhang Z, Shi G, Fang X, Wang L, Gao X, Fang Y, Xu T, Wang S, Liu X. Review on thermal management systems using phase change materials for electronic components, Li-ion batteries and photovoltaic modules. Renewable and Sustainable Energy Reviews, 2014, 31: 427-438.

[22] Alipanah M, Li X. Numerical studies of lithium-ion battery thermal management systems using phase change materials and metal foams. International Journal of Heat and Mass Transfer, 2016, 102: 1159-1168.

[23] Wilke S, Schweitzer B, Khateeb S, Al-Hallaj S. Preventing thermal runaway propagation in lithium ion battery packs using a phase change composite material: An experimental study. Journal of Power Sources, 2017, 340: 51-59.

[24] Azizi Y, Sadrameli SM. Thermal management of a LiFePO 4 battery pack at high temperature environment using a composite of phase change materials and aluminum wire mesh plates. Energy Conversion and Management, 2016, 128: 294-302.

[25] Wu W, Yang X, Zhang G, Chen K, Wang S. Experimental investigation on the thermal performance of heat pipe-assisted phase change material based battery thermal management system. Energy Conversion and Management, 2017, 138: 486-492.

[26] Jiang G, Huang J, Liu M, Cao M. Experiment and simulation of thermal management for a tube-shell Li-ion battery pack with composite phase change material. Applied Thermal Engineering, 2017, 120: 1-9.

[27] Zou H, Wang W, Zhang G, Qin F, Tian C, Yan Y. Experimental investigation on an integrated thermal management system with heat pipe heat exchanger for electric vehicle. Energy Conversion and Management, 2016, 118: 88-95.

[28] Lazrak A, Fourmigué JF, Robin JF. An innovative practical battery thermal management system based on phase change materials: Numerical and experimental investigations. Applied Thermal Engineering, 2017.

[29] Rao Z, Wang Q, Huang C. Investigation of the thermal performance of phase change material/mini-channel coupled battery thermal management system. Applied Energy, 2016, 164: 659-669.

[30] Ng K S, Moo C S, Chen Y P, Hsieh Y C. Enhanced coulomb counting method for estimating state-of-charge and state-of-health of lithium-ion batteries. Applied energy, 2009, 86(9): 1506-1511.

[31] Y. He. Rapid thermal conductivity measurement with a hot disk sensor: Part 1. Theoretical considerations. Thermochimica Acta, 2005, 436: 122-129.

[32] Tiari S, Qiu S, Mahdavi M. Numerical study of finned heat pipe-assisted thermal energy storage system with high temperature phase change material. Energy Conversion and Management, 2015, 89: 833-842.

[33] Tan F L, Hosseinizadeh S F, Khodadadi J M, Fan L W. Experimental and computational study of constrained melting of phase change materials (PCM) inside a spherical capsule. International Journal of Heat and Mass Transfer, 2009, 52(15): 3464-3472.

[34] Bernardi D, Pawlikowski E, Newman J. A general energy balance for battery systems. Journal of the Electrochemical Society, 1984, 132(1):5-12.

[35] Shi S, Xie Y Q, Li M, Yuan Y P, Yu J Z, Wu H W, Liu B, Liu N. Non-steady experimental investigation on an integrated thermal management system for power battery with phase change materials. Energy Conversion and Management, 2017, 138: 84-96.

[36] Zhao R, Gu J, Liu J. Optimization of a phase change material based internal cooling system for cylindrical Li-ion battery pack and a hybrid cooling design. Energy, 2017, 135: 811-822.